Mutual-Information Based Optimal Experimental Design for Hyperpolarized ^{13}C-Pyruvate MRI[*]

Prashant K. Jha[†1], Christopher Walker[‡2], Drew Mitchell[§2], J. Tinsley Oden[¶1], Dawid Schellingerhout[‖2], James A. Bankson[**2], and David T. Fuentes[††2]

[1] *Oden Institute for Computational Engineering and Sciences, The University of Texas at Austin, Austin, TX 78712, USA*
[2] *Department of Imaging Physics, MD Anderson Cancer Center, Houston, TX 77320, USA*

June 28, 2022

Abstract

Background. Hyperpolarized (HP) ^{13}C-Pyruvate MR imaging provides unique information about metabolic alterations indicative of the aggressiveness of certain cancer types. The information content of the HP-MRI data is fundamentally limited by the physics and chemistry of specific processes that take place at an atomic scale during a well-defined chemical reaction. The HP signal (magnetization of pyruvate and lactate) is a fixed resource that is established at the polarizer and naturally decays over time, and cannot be renewed after injection. The signal is further reduced with every radio-frequency excitation by the MR pulse sequence. Therefore, optimal experimental design (OED) for data acquisition is fundamentally important. A key parameter of interest recovered from HP-MRI measurements is the apparent pyruvate-to-lactate exchange rate, k_{PL}, for measuring tumor metabolism. This manuscript presents an information-theory-based OED approach that minimizes the uncertainty in the rate parameter, k_{PL}, recovered from the HP-MRI measurements.

Methods. Mutual information (MI) is a statistical property employed here to measure the information content of the HP measurements with respect to the first-order exchange kinetics of the pyruvate conversion to lactate. An optimal experimental design formulation based on the maximization of the mutual information as a function of the MRI design parameters is proposed. The optimized MRI design parameters include flip angles of the pulse sequence acquisition. Further, a spatially varying model (high-fidelity) based on the Block – Torrey equations is proposed and utilized as a control for the OED formulation.

Results. Within the mutual-information-based optimal experimental design formulation, a time-varying flip angle scheme is seen to provide significant differences in the flip angles compared to when excitation angles are fixed to a constant value. The varying flip angle scheme leads to a higher parameter optimization that can further improve the quantitative value of mutual information over the constant flip angle scheme. However, the constant flip angle scheme leads to the best accuracy and precision when considering inference from noise-corrupted data.

Conclusion. Results suggest that the mutual information-based optimal data acquisition strategy is likely to improve the precision of the measurements. For the particular MRI data examined here, pyruvate and lactate flip angles of 35 and 28 degrees, respectively, were the best choice in terms of accuracy and precision of the parameter recovery. Moreover, the recovery of rate parameter k_{PL} from the data generated from the high-fidelity model highlights the influence of diffusion and strength of vascular source on the recovered rate parameter. Since the existing pharmacokinetic models for HP-MRI do not account for spatial variation, the optimized design parameters may not be fully optimal in a more general 3D setting.

1 Introduction

The potential of hyperpolarized ^{13}C-Pyruvate magnetic resonance imaging (HP-MRI) to characterize cancer biology, predict progression, and monitor early responses to treatment is well known (e.g., [1–9]). Ongoing studies in

---

[*]Corresponding authors: Prashant K. Jha (prashant.jha@austin.utexas.edu) and David T. Fuentes(dtfuentes@mdanderson.org)

[†]prashant.jha@austin.utexas.edu

[‡]cmwalker@mdanderson.org

[§]DMitchell2@mdanderson.org

[¶]oden@oden.utexas.edu

[‖]dawid.schellingerhout@mdanderson.org

[**]jbankson@mdanderson.org

[††]dtfuentes@mdanderson.org

prostate, brain, breast, liver, cervical, and ovarian cancer [1, 3, 4] have shown that HP ^{13}C-Pyruvate MRI is safe and effective. One of the central aspects of HP-MRI that make it appealing is the elevated chemical conversion of pyruvate to lactate, even in the presence of oxygen, via lactate dehydrogenase (LDH), also referred to as the Warburg effect [10, 11]. The higher production of lactate has been shown to correlate with disease presence, the aggressiveness of the disease (e.g., cancer and inflation), and response to therapy. The rate of pyruvate-to-lactate exchange (k_{PL}) is a crucial parameter of interest in locating aggressive disease and assessing the biological state of the tissue. HP-MRI presents a unique opportunity to observe tumor metabolism *in vivo* [2, 3, 5, 6] and use this information to make inferences about tumor aggressiveness and response to therapy. However, a recent white paper [3] highlights the need for further development of spatial, temporal, and spectral encoding strategies that minimize uncertainty while maximizing the efficiency of HP-MRI. An example of uncertainty is the variability of the reported HP measurements in the literature [12–14]. In the present work, we develop an information-theory-based approach to determine the optimal MRI design parameters, such as flip angles, with a goal of reducing the uncertainty in the recovered rate parameter, k_{PL}.

HP ^{13}C-pyruvate MRI scans consist of several steps [3, 5]; first, a mixture is prepared consisting of ^{13}C-enriched metabolites ($[1-^{13}C]$-pyruvate) and an electron paramagnetic agent (EPA) that mediates polarization buildup and transfer. Using the Dynamic Nuclear Polarization (DNP) method, one of the atoms of the ^{13}C-pyruvate molecule is polarized heavily; $[1-^{13}C]$-pyruvate means that the first carbon is labeled with the ^{13}C isotope, which is visible by magnetic resonance (MR). On the other hand, 98.9 percent of the carbon are ^{12}C which has a spin quantum number of zero and therefore can not be polarized or detected by MR. Once the mixture is processed to obtain the hyperpolarized pyruvate, the temperature of the solution is brought to the body temperature and quickly injected into the patient. Following the injection, the patient is scanned using a gradient echo pulse sequence to measure the temporal evolution of the ^{13}C-pyruvate and ^{13}C-lactate (lactate produced from hyperpolarized pyruvate too are visible in the scan) magnetizations. The artificial polarization of ^{13}C-pyruvate (and ^{13}C-lactate) decays rapidly, and therefore the injection and subsequent MR scans must be performed quickly, within $100 - 160$ seconds. One of the critical reasons for using ^{13}C-pyruvate is its compatibility; it is an endogenous substance that plays a central role in catabolic and anabolic metabolism. The repetition time of the MR pulse sequence is limited by the number of slices and relaxation (decay) of polarized molecules, typically above 0.5 and below $5-10$ seconds. The key scan parameter at each scan is the flip angle (or excitation angle); a larger flip angle provides a higher signal (the magnetization of pyruvate and lactate) intensity; however, the signal that remains for the following scan is reduced. Therefore, the choice of flip angles can impact the quality of data and, thus, the quality of the recovered parameter. There are other design parameters that can be considered, for example, spectral encoding scheme, gradient trajectory, etc. However, in this work, the flip angles for pyruvate and lactate are chosen as design parameters.

The time history of pyruvate and lactate magnetization within the imaging voxels constitutes the data of interest. Together with a pharmacokinetic HP-MRI model, pyruvate and lactate magnetization data are employed to recover the pyruvate-to-lactate apparent exchange rate, k_{PL}; e.g., [2, 15, 16]. Accuracy and uncertainty in the recovered rate parameter depend on the data's information content and the pharmacokinetic model's fidelity. This work aims to determine the MRI design parameters that increase the information content in the data and reduce the uncertainty in the rate parameter. The mutual information (MI) between the data and critical model parameters is utilized toward this goal. Information theory and, specifically, mutual information provides a rigorous mathematical framework to identify optimal MR imaging data and acquisition parameters that maximize image reconstruction quality. It offers a quantitative methodology for optimizing acquisition protocols to improve reproducibility.

To verify the reduction in uncertainty of recovered rate parameter k_{PL} using optimal design parameters, we generate synthetic data from low-fidelity pharmacokinetic and high-fidelity models. The high-fidelity model is obtained using continuum mixture theory and includes two linear coupled partial differential equations for spatially varying HP pyruvate and lactate in the tissue. It is shown that for data from both models, optimal design parameters reduce uncertainty in the pyruvate-to-lactate apparent exchange rate, k_{PL}.

The article is structured as follows: In Section 2 related work is reviewed. Section 3 presents the pharmacokinetic and high-fidelity models used to produce data for verification of optimal scan parameters. The optimization of scan parameters based on mutual information is discussed in Section 4. The results obtained from the proposed model are presented in Section 5. In Section 6 some conclusions are drawn, and future directions are proposed. The codes and relevant files to reproduce the results will be publicly available in the following GitHub repository: `https://github.com/prashjha/HyperpolarizedMRI`.

2 Related works

Formulating optimal HP acquisition strategies is challenging and tightly coupled with the analysis of appropriate models of MRI physics. Semi-quantitative metrics such as the ratio of the integrals of the lactate-to-pyruvate signals (area under the curve, AUC) are often preferred due to their simplicity. However, the lactate-to-pyruvate ratio is biased by HP pyruvate in blood vessels that are inaccessible to enzymes that mediate conversion from HP pyruvate to lactate. For example, if the vascular blood volume decreases by 10 percent in a region of a tumor, the lactate-to-pyruvate ratio could increase even if the true metabolic state of cells does not change. The lactate-to-pyruvate ratio is also affected by the excitation scheme. Small flip angles consume less pyruvate magnetization and permit the signal pool to remain longer for the conversion to lactate. The potential for variability is realized in the literature. In applications to brain cancer (glioma) Grist [12] reports a lactate to pyruvate ratio of .25 ± .08 and .22 ± .06 in white matter and gray matter, respectively. Lactate-to-pyruvate ratios greater than 1.0 are reported in [13] in gray matter. Lactate-to-pyruvate ratios in white matter of 0.43 ± 0.14 (32-channel) were reported in [14].

The information theoretic approach developed in this work is an extension of optimal experimental design approaches that use the Fisher information matrix and the Cramer – Rao bound as a lower bound on the variance of unbiased estimators [16–24]. Indeed, the de Bruijn identity [25] provides a direct connection between derivatives of our entropy calculations and the Fisher information matrix. However, optimizing the Fisher information matrix requires estimates of the unknown tissue parameters, such as T_1 relaxation losses and pyruvate-to-lactate conversion rate (that we are trying to recover), to calculate the Fisher information. The Fisher information must be iteratively re-optimized as more accurate estimates of the tissue properties are obtained. In contrast, the present approach provides a mathematical framework to directly include the tissue parameter uncertainty in the mutual information and considers a range of tissue parameters (determined by the input probability distributions) to calculate and optimize the mutual information.

3 Hyperpolarized (HP) MRI model

Consider a tissue domain within which different constituents evolve depending on the local environment which includes, for example, interstitial, vascular, and cellular spaces. In this work, following [2, 15], two spatial compartments, namely, interstitial and vascular, each containing HP pyruvate and lactate and complement of these two constituents, are considered. First, the spatially invariant pharmacokinetic model developed in [15] is presented. The model accounts for T_1 relaxation loss, signal loss due to excitation at each scan, and pyruvate-to-lactate and lactate-to-pyruvate exchanges. This model is referred to as the low-fidelity (LF) model for convenience. To generate synthetic data as a control to test optimal design parameters, the low-fidelity model is extended using principles of continuum mixture theory to obtain a PDE-based model, referred to as the high-fidelity (HF) model. The HF model includes the vascular-tissue exchange in an attempt to produce a more accurate perfusion of HP pyruvate. The two models are presented next.

3.1 Spatially invariant HP-MRI low-fidelity (LF) model

A two compartment HP-MRI model (interstitial and vascular) consisting of two constituents, HP pyruvate and lactate, is considered.

Let $\bar{\phi}_P = \bar{\phi}_P(t)$ and $\bar{\phi}_L = \bar{\phi}_L(t)$ denote the average volume fraction of HP pyruvate and lactate, respectively, over the tissue domain $\Omega \subset \mathbb{R}^3$ at time $t \in [0, T]$. Discrete times at N scans are denoted by t_k, $1 \leq k \leq N$; θ_P^k and θ_L^k are flip angles in k^{th} scan whereas $TR_k = t_k - t_{k-1}$, $k > 1$, are repetition times and $TR_1 = 0$. With $\bar{\phi} = (\bar{\phi}_P, \bar{\phi}_L)^T$, the HP pyruvate and lactate available for measurement at the $(k+1)^{\text{th}}$ scan, $k \geq 1$, are given by [15]

$$\bar{\phi}(t_{k+1}) = \exp\left[TR_{k+1}\boldsymbol{A}\right]\boldsymbol{C}^k\bar{\phi}(t_k) + \frac{k_{ve}}{\nu_e}\int_{t_k}^{t_{k+1}} \exp\left[(t_{k+1} - \tau)\boldsymbol{A}\right]\boldsymbol{VIF}(\tau)d\tau, \tag{1}$$

where the matrix $\boldsymbol{A}$ accounts for T_1 relaxation losses and pyruvate-lactate exchanges

$$\boldsymbol{A} = \begin{bmatrix} -\frac{1}{T_{1,P}} - k_{PL} - \frac{k_{ve}}{\nu_e} & k_{LP} \\ k_{PL} & -\frac{1}{T_{1,L}} - k_{LP} \end{bmatrix}. \tag{2}$$

Here $T_{1,P}, T_{1,L}$ denote the T_1 relaxation times (s), k_{PL}, k_{LP} pyruvate-to-lactate and lactate-to-pyruvate exchange rates (s^{-1}), k_{ve} vascular-tissue exchange rate (s^{-1}), and ν_e the extravascular volume fraction. In (1), $\boldsymbol{C}^k$ denotes

the matrix that takes into account the loss of signal due to excitation at k^{th} scan:

$$\boldsymbol{C}^k = \begin{bmatrix} \cos(\theta_P^k) & 0 \\ 0 & \cos(\theta_L^k) \end{bmatrix}. \tag{3}$$

Lastly, $\boldsymbol{VIF} = \boldsymbol{VIF}(t)$ is the vascular input function assumed to take the form:

$$\boldsymbol{VIF}(t) = \begin{bmatrix} \sigma_P \gamma(t - \bar{t}_0, \alpha_P, \beta_P) \\ 0 \end{bmatrix}, \tag{4}$$

where $\sigma_P, \alpha_P, \beta_P$ are constants, and γ denotes a gamma probability density function given by

$$\gamma(t, a, b) = \frac{1}{b^a \Gamma(a)} t^{a-1} \exp\left[-\frac{t}{b}\right]. \tag{5}$$

The constant $\bar{t}_0$ is associated with bolus arrival time and is treated as one of the uncertain model parameters.

In (1), the parameters can be gathered in two different classes: 1) model parameters that depend on the tissue domain and includes $\mathcal{P} = (T_{1,P}, T_{1,L}, k_{PL}, k_{LP}, k_{ve}, \nu_e, \bar{t}_0)$, and 2) HP MRI design parameters such as repetition times and flip angles $\mathcal{K} = (\{TR_i\}_{i=2}^N, \{\theta_P^i\}_{i=1}^N, \{\theta_L^i\}_{i=1}^N)$. For simplicity, the parameters $T_{1,P}, T_{1,L}, \nu_e, k_{LP}$ are assumed to be known and fixed so that $\mathcal{P} = (k_{PL}, k_{ve}, \bar{t}_0)$. Repetition times TR_k are also considered fixed so that $\mathcal{K} = (\{\theta_P^i\}_{i=1}^N, \{\theta_L^i\}_{i=1}^N)$.

3.1.1 The total signal

For simplicity, let $\bar{\boldsymbol{\phi}}^k = \bar{\boldsymbol{\phi}}(t_k)$, $\bar{\phi}_P^k = \bar{\phi}_P(t_k)$, $\bar{\phi}_L^k = \bar{\phi}_L(t_k)$, where $k = 1, 2, ..., N$. Suppose prior to the kth scan, the available HP pyruvate signal is $\bar{\phi}_P^k$. After taking the kth scan, due to signal excitation loss, $\cos(\theta_P^k)\bar{\phi}_P^k$ will be available for the next measurement. A similar argument can be made for $\bar{\phi}_L^k$. Further, the signals measured at the kth scan are, see [15],

$$\boldsymbol{s}^k = \begin{bmatrix} s_P^k \\ s_L^k \end{bmatrix} = \begin{bmatrix} \sin(\theta_P^k) & 0 \\ 0 & \sin(\theta_L^k) \end{bmatrix} \left(\nu_e \bar{\boldsymbol{\phi}}^k + (1 - \nu_e)\boldsymbol{VIF}(t_k)\right) = \begin{bmatrix} \sin(\theta_P^k)\left(\nu_e \bar{\phi}_P^k + (1 - \nu_e)\boldsymbol{VIF}_1(t_k)\right) \\ \sin(\theta_L^k)\left(\nu_e \bar{\phi}_L^k + (1 - \nu_e)\boldsymbol{VIF}_2(t_k)\right) \end{bmatrix} \tag{6}$$

i.e., one only measures the $\sin(\theta_P^k)$ and $\sin(\theta_L^k)$ fractions of the magnetization leaving the $\cos(\theta_P^k)$ and $\cos(\theta_L^k)$ fractions for the next measurement. The total signal is the sum of the individual signals at different scans and is given by

$$\mathcal{G} = \mathcal{G}(\mathcal{K}, \mathcal{P}) = \sum_{k=1}^N \left(s_P^k + s_L^k\right), \tag{7}$$

where the dependence of $\mathcal{G}$ on the design parameters $\mathcal{K}$ and model parameters $\mathcal{P}$ is clear from (1) and (6).

3.2 HP-MRI high-fidelity (HF) model for data generation

The verification of uncertainty reduction in recovered k_{PL} on living subjects using the optimal design parameters is a challenging undertaking. One approach for verification is to use the synthetic data generated from the computational models. Here, the two models are employed to generate synthetic data; the first model is the same ODE model described in previous section. As a second model, somewhat more realistic model that includes spatial variation of the HP pyruvate and lactate is developed using the principles of continuum mixture theory and invoking the principle of conservation of mass; see [26–29].

Let $\Omega \subset \mathbb{R}^3$ be an open bounded domain representing a tissue. At any $\boldsymbol{x} \in \Omega$, consider an RVE (Representative Volume Element at sub-tissue-scale (≈ 1 mm). At this scale, a typical RVE may include three compartments: *interstitial*, *vascular*, and *cellular*. These compartments may host various constituents, e.g., proteins, plasma, etc., and constituents can interact with other and exchange mass at the interfaces between compartments. Of particular interest in this work are the HP pyruvate and lactate in interstitial and vascular compartments. Following some simplifying assumptions outlined in Appendix A, the evolution of pyruvate and lactate volume fractions, $\phi_P = \phi_P(t, \boldsymbol{x})$ and $\phi_L = \phi_L(t, \boldsymbol{x})$, $t \in (0, t_F)$, $\boldsymbol{x} \in \Omega$, in interstitial compartment can be described by a coupled system of reaction-diffusion partial differential equations. HP agents in vascular compartments, denoted by $\phi_{PV} = \phi_{PV}(t, \boldsymbol{x})$ for HP pyruvate and $\phi_{LV} = \phi_{LV}(t, \boldsymbol{x})$ for lactate, $t \in (0, t_F), \boldsymbol{x} \in \Omega$, are assumed to be fixed and given as a function of time and space.

To account for the instantaneous loss of signal (or volume fractions) of HP agents at discrete scan points t_k, $1 \leq k \leq N$, consider $\phi_A^k = \phi_A^k(t, \boldsymbol{x})$, where $t \in [t_{k-1}, t_k)$, $\boldsymbol{x} \in \Omega$, $A \in \{P, L, PV, LV\}$. The balance of mass for constituents

4

in interstitium based on simplifying assumptions can be expressed in differential form, for $t \in (t_{k-1}, t_k), \boldsymbol{x} \in \Omega$, as follows

$$
\begin{aligned}
\frac{\partial}{\partial t}\phi_P^k &= \nabla \cdot \left(D_P \nabla \phi_P^k\right) + S_P(\phi_P^k, \phi_L^k) + J_P(\phi_P^k, \phi_{PV}^k), \\
\frac{\partial}{\partial t}\phi_L^k &= \nabla \cdot \left(D_L \nabla \phi_L^k\right) + S_L(\phi_P^k, \phi_L^k) + J_L(\phi_L^k, \phi_{LV}^k),
\end{aligned}
\tag{8}
$$

where D_P, D_L are diffusivities of pyruvate and lactate, $S_P = S_P(\phi_P^k, \phi_L^k), S_L = S_L(\phi_P^k, \phi_L^k)$ volume source terms, and $J_P = J_P(\phi_P^k, \phi_{PV}^k), J_L = J_L(\phi_L^k, \phi_{LV}^k)$ vascular-interstitial volume exchange terms. The initial condition for the HP pyruvate and lactate, ϕ_P^k, ϕ_L^k, should take into account the loss of signal due to excitation in the $(k-1)^{\text{th}}$ scan. For example, HP pyruvate just before the $(k-1)^{\text{th}}$ scan is $\phi^{k-1}(t_{k-1})$, and the available signal due to instant loss of signal after $(k-1)^{\text{th}}$ scan is $\cos(\theta_P^{k-1})\phi_P^{k-1}(t_{k-1})$. Based on the above argument, initial conditions are taken as

$$
\phi_P^k(t_{k-1}, \boldsymbol{x}) = \cos(\theta_P^{k-1})\phi_P^{k-1}(t_{k-1}, \boldsymbol{x}), \quad \phi_L^k(t_{k-1}, \boldsymbol{x}) = \cos(\theta_L^{k-1})\phi_L^{k-1}(t_{k-1}, \boldsymbol{x}), \qquad \forall \boldsymbol{x} \in \Omega, 1 \le k \le N. \tag{9}
$$

Homogeneous Neumann boundary conditions are assumed to hold, i.e.,

$$
\nabla \phi_P^k(t, \boldsymbol{x}) \cdot \boldsymbol{n} = 0, \quad \nabla \phi_L^k(t, \boldsymbol{x}) \cdot \boldsymbol{n} = 0, \qquad \forall t \in [t_{k-1}, t_k], \boldsymbol{x} \in \partial\Omega, \tag{10}
$$

where $\boldsymbol{n}$ is the unit outward normal of the boundary $\partial\Omega$. For the well-posedness of (9) for $k=1$, it is assumed that $\phi_P^0(t_0, \boldsymbol{x}) = \phi^0(t_0, \boldsymbol{x}) = 0$, for all $\boldsymbol{x} \in \Omega$, and $\theta_P^0 = \theta_L^0 = 0$.

The volume source terms S_P, S_L are defined as follows:

$$
S_P(\phi_P^k, \phi_L^k) = \left(-\frac{1}{T_{1,P}} - k_{PL}\right)\phi_P^k + k_{LP}\phi_L^k, \qquad S_L(\phi_P^k, \phi_L^k) = \left(-\frac{1}{T_{1,L}} - k_{LP}\right)\phi_L^k + k_{PL}\phi_P^k, \tag{11}
$$

and the tissue-vascular volume exchange terms are simply taken as the volume sources restricted on vascular subdomain, $\Omega_V \subset \Omega$, i.e.,

$$
J_P(\phi_P^k, \phi_{PV}^k) = L_P \phi_{PV}^k \chi_{\Omega_V}, \qquad J_L(\phi_L^k, \phi_{LV}^k) = L_L \phi_{LV}^k \chi_{\Omega_V}, \tag{12}
$$

where χ_A is the characteristics function of set A, i.e., $\chi_A(\boldsymbol{x}) = 1$ if $\boldsymbol{x} \in A$ and $\chi_A(\boldsymbol{x}) = 0$ if $\boldsymbol{x} \notin A$, and L_P, L_L permeabilities.

HP agents in the vascular compartment are fixed as, for all $t \in [t_k, t_{k+1})$,

$$
\phi_{PV}^k(t, \boldsymbol{x}) = \begin{cases} \sigma_P \gamma(t - \bar{t}_0, \alpha_P, \beta_P), & \text{if } \boldsymbol{x} \in \Omega_V, \\ 0, & \text{otherwise} \end{cases} \tag{13}
$$

and $\phi_{LV}^k(t, \boldsymbol{x}) = 0, \forall \boldsymbol{x} \in \Omega$. Here $\bar{t}_0, \sigma_P, \alpha_P, \beta_P$ are constants that control the magnitude and shape of the gamma function γ defined in (5).

Next, the model is presented. Further details about the setup of this model and simplifying assumptions are provided in Appendix A.

3.2.1 Signal from the high-fidelity model

The magnetization intensity of constituent A, $A \in \{P, L, PV, LV\}$, at $\boldsymbol{x} \in \Omega$ at k^{th} scan is assumed to be proportional to the volume fraction of the constituent, ϕ_A^k, i.e., there are constants C_A, $A \in \{P, L, PV, LV\}$, such that $C_A \sin(\theta_A^k)\phi_A^k(t_k, \boldsymbol{x})$ is the measured signal of constituent A at the kth scan. Here, $\theta_{PV}^k = \theta_P^k$ and $\theta_{LV}^k = \theta_L^k$, where θ_P^k, θ_L^k are the flip angles. Without loss of generality, it is assumed that $C_A = 1$, for $A \in \{P, L, PV, LV\}$.

4 Mutual information based optimization of MR scan parameters

A major goal of this study is to formulate a optimization problem to determine the design parameters $\mathcal{K} = (\{\theta_P^i\}_{i=1}^N, \{\theta_L^i\}_{i=1}^N)$ such that the MRI measurements reduce uncertainty in the rate parameter, k_{PL}. Treating total signal, $\mathcal{G}$ defined in (7), as the data, and model parameters, $\mathcal{P} = (k_{PL}, k_{ve}, \bar{t}_0)$, together with data as random variables, an optimization problem of maximizing the mutual information (MI) between the data and model parameters is proposed. It is shown that uncertainty in recovered k_{PL} from synthetic noisy data is reduced when optimal design parameters are considered; see Section 5.

In what follows, after defining some preliminary quantities, the mutual information between data and the model parameters is defined. Let $z \in Z = \mathbb{R}$, $\mathcal{P} \in \Theta \subset \mathbb{R}^3$, and $\mathcal{K} \in D \subset \mathbb{R}^{2N}$, where Z, Θ, D are data, model parameter, and design parameter spaces, respectively.

4.1 Prior, likelihood, and evidence

Suppose $p_0(\mathcal{P})$ is the prior probability distribution function (PDF) of model parameters $\mathcal{P}$ and $p(z)$ is the PDF of the data z. Then the joint PDF $p(z, \mathcal{P})$ must satisfy

$$p(z, \mathcal{P}) = p(z|\mathcal{P})p_0(\mathcal{P}) = p(\mathcal{P}|z)p(z), \tag{14}$$

where $p(z|\mathcal{P})$ is the conditional PDF of data conditioned on model parameters $\mathcal{P}$ (also referred to as the *likelihood* function) and $p(\mathcal{P}|z)$ the conditional PDF of model parameters $\mathcal{P}$ conditioned on data z (*posterior* of $\mathcal{P}$). The prior is taken as multi-variate Gaussian with mean $\hat{\mathcal{P}}$ and covariance matrix $\Sigma_{\mathcal{P}}$:

$$\mathcal{P} \sim p_0(\mathcal{P}) = \mathcal{N}(\hat{\mathcal{P}}, \Sigma_{\mathcal{P}}) = \frac{1}{2\pi \det \Sigma_{\mathcal{P}}} \exp\left(-\frac{1}{2} \|\hat{\mathcal{P}} - \mathcal{P}\|^2_{\Sigma_{\mathcal{P}}^{-1}} \right). \tag{15}$$

Here $\|\hat{\mathcal{P}} - \mathcal{P}\|^2_{\Sigma_{\mathcal{P}}^{-1}} = (\hat{\mathcal{P}} - \mathcal{P}) \cdot \Sigma_{\mathcal{P}}^{-1}(\hat{\mathcal{P}} - \mathcal{P})$. Within this Bayesian setting, Σ_p, is representative of biological variability.

To derive the expression for the likelihood function, first suppose that $\mathcal{G} = \mathcal{G}(\mathcal{K}, \mathcal{P})$ is the model prediction of data. Data and the model prediction are assumed to be related as follows:

$$z = \mathcal{G}(\mathcal{K}, \mathcal{P}) + \varepsilon \quad \Rightarrow \quad z - \mathcal{G}(\mathcal{K}, \mathcal{P}) \sim \mathcal{N}(0, \sigma_z), \tag{16}$$

where an additive model of noise is assumed and the noise, ε, is taken as Gaussian with a zero mean and standard deviation σ_z, i.e., $\varepsilon \sim \mathcal{N}(0, \sigma_z^2)$.

Therefore, the likelihood function $p(z|\mathcal{P})$ takes the Gaussian form:

$$p(z|\mathcal{P}) = \mathcal{N}(\mathcal{G}(\mathcal{K}, \mathcal{P}), \sigma_z) = \frac{1}{2\pi\sigma_z} \exp\left(-\frac{1}{2\sigma_z^2} \|\mathcal{G}(\mathcal{K}, \mathcal{P}) - z\|^2 \right). \tag{17}$$

Here $\| \cdot \|$ denotes the Euclidean norm. Technically, $p(z|\mathcal{P})$ is also conditioned on $\mathcal{K}$, but, for simplicity in notation, the dependence on $\mathcal{K}$ is suppressed.

With $p_0(\mathcal{P})$ and $p(z|\mathcal{P})$ defined as above, the joint PDF $p(z, \mathcal{P})$ can be computed using (14). Further, using (14), the PDF of data z (evidence), $p(z)$, can be computed by marginalizing $p(z, \mathcal{P})$ with respect to $\mathcal{P}$:

$$p(z) = \int_{\Theta} p(z, \mathcal{P}) d\mathcal{P} = \int_{\Theta} p(z|\mathcal{P}) p_0(\mathcal{P}) d\mathcal{P}, \tag{18}$$

where Θ is the parameter space.

4.2 Mutual information

Next, the statistical mutual information is defined and the optimization problem for design parameters $\mathcal{K}$ is posed. Given HP-MRI data, the accurate inference of pyruvate-to-lactate exchange rate parameters (and other parameters in $\mathcal{P}$) depends on the specific choice of control (design) parameters $\mathcal{K}$ as selection of $\mathcal{K}$ affects the information content in the measured data. The notion of mutual information [25] provides a way to quantify the information content about the model parameters $\mathcal{P}$ in the data z. The mutual information between the two random variables z and $\mathcal{P}$ with PDFs $p(z)$ and $p_0(\mathcal{P})$ and the joint PDF $p(z, \mathcal{P})$ is defined as

$$I = I(\mathcal{K}) = \int_Z \int_{\Theta} p(z, \mathcal{P}) \ln\left(\frac{p(z, \mathcal{P})}{p_0(\mathcal{P})p(z)} \right) d\mathcal{P}dz. \tag{19}$$

Here, the mutual information I depends only on design parameters $\mathcal{K}$ and the forward model (1).

Using Bayes theorem, $p(z, \mathcal{P}) = p(z|\mathcal{P})p_0(\mathcal{P})$, it can easily be shown that

$$I(\mathcal{K}) = \int_Z \int_{\Theta} p(z|\mathcal{P})p_0(\mathcal{P}) \ln\left(\frac{p(z|\mathcal{P})p_0(\mathcal{P})}{p_0(\mathcal{P})p(z)} \right) d\mathcal{P}dz, \tag{20}$$

or,

$$I(\mathcal{K}) = \int_Z \int_{\Theta} p(z|\mathcal{P})p_0(\mathcal{P}) \ln\left[p(z|\mathcal{P}) \right] d\mathcal{P}dz - \int_Z p(z) \ln p(z) dz = H(z; \mathcal{K}) - H(z|\mathcal{P}; \mathcal{K}), \tag{21}$$

where the second term in the above equation is identified as information entropy $H(z; \mathcal{K})$ and the first term as negative of the cross-information entropy, $H(z|\mathcal{P}; \mathcal{K})$. That is

$$H(z; \mathcal{K}) = -\int_Z p(z) \ln p(z) dz, \qquad H(z|\mathcal{P}; \mathcal{K}) = -\int_Z \int_{\Theta} p(z|\mathcal{P})p_0(\mathcal{P}) \ln\left[p(z|\mathcal{P}) \right] d\mathcal{P}dz. \tag{22}$$

Optimization problem In order to maximize the reduction in the uncertainty in the model parameters (i.e. to have the most confident estimates of the parameters $\mathcal{P}$), we propose to maximize the mutual information between the observation data and parameters of interest:

$$\max_{\mathcal{K} \in D} I(\mathcal{K}) = I(\mathcal{K}^*), \tag{23}$$

where $\mathcal{K}^*$ is the design parameter for which I is maximum (assuming $\mathcal{K}$ exist).

Given a Gaussian prior and conditional probability of the data with respect to the parameters, the entropy of the data conditioned on the model parameter, i.e., $H(z|\mathcal{P})$, is constant. Therefore, the optimization problem simplifies to

$$\mathcal{K}^* = \operatorname*{argmax}_{\mathcal{K} \in D} I(\mathcal{K}) = \operatorname*{argmax}_{\mathcal{K} \in D} H(z; \mathcal{K}). \tag{24}$$

4.3   Approximation of mutual information and information entropy

Mutual information calculations are computationally demanding due to high-dimensional integration over the parameter and data spaces. Combinations of both quadrature and sampling methods have been employed for mutual information calculations, each of which is well-suited to certain function classes [30–42]. These methods include Monte Carlo and Quasi-Monte Carlo methods [31–33], lattice rules [34], adaptive subdivision [35,36], neural network approximations [37] and numerical quadrature [38]. Here the problem structure is used to accelerate computations and facilitate tractable numerical integration. Following [43], Gauss-Hermite quadrature is applied in each dimension of mutual information integrals defined in (21) to numerically integrate multi-variate Gaussian random variables. Quadrature order is increased until convergence is observed.

5   Numerical results

In this section, the main results of our analysis are presented. First, the optimal design parameters for different signal-to-noise ratios (SNRs) are shown. Optimal design parameters for both temporally constant and varying flip angles at each data acquisition are considered. Next, the reduction in uncertainty of k_{PL} when using optimal design parameters generated synthetic data is shown; synthetic data are generated using the two models discussed in Section 3.

For the optimization of mutual information and inverse problem to recover model parameters from the noisy data, the automatic differentiation feature in MATLAB is utilized. Details on the numerical solution of the low and high-fidelity models are given in Appendix B. The values of model parameters and MR scan (design) parameters are listed in Tables 1 and 2, respectively.

Parameter	Value	Description
L_P, L_L	0.2 s^{-1}	Permeabilities for vessel-tissue mass exchange (only for HF model)
D_P, D_L	20 cm^2/s^{-1}	Diffusivities (only for HF model)
$T_{1,P}, T_{1,L}$	30 s, 25 s	Relaxation times
k_{PL}	0.15 s^{-1}	Pyruvate-to-lactate apparent exchange rate
k_{LP}	0 s^{-1}	Lactate-to-pyruvate apparent exchange rate
$\bar{t}_0$	4 s	Bolus arrival time for HP pyruvate
$\sigma_P, \alpha_P, \beta_P$	100, 2.5, 4.5 s	Parameters in the gamma function (13)
k_{ν_e}	0.05 s^{-1}	vascular-tissue exchange rate (only for LF model)
ν_e	0.95	extravascular volume fraction (only for LF model)

Table 1: Default model parameters, $\mathcal{P}$, and remaining fixed model parameters used in initialization, optimization, and verification steps. Some parameters are specific to either LF (low-fidelity) or HF (high-fidelity) model while the rest are the same in the two models. The parameters such as D_P, D_L, L_P, L_L for HF model are assumed arbitrary values without loss of generality.

Parameter	Value	Description
N	30	Number of HP MRI scans
TR_k	3 s	Repetition times (for $k > 1$)
θ_P^k	20 degrees	Flip angles for HP pyruvate (for all k)
θ_L^k	30 degrees	Flip angles for HP lactate (for all k)

Table 2: Default design parameters, $\mathcal{K}$, used in initialization, optimization, and verification steps.

5.1 Optimized design parameters

As mentioned in Section 4, multi-variate Gaussian is taken as a prior for uncertain model parameters, $\mathcal{P} = (k_{PL}, k_{ve}, \bar{t}_0)$. The mean and diagonal covariance matrix are fixed to

$$\mu_{\mathcal{P}} = (0.15, 0.05, 4), \qquad \Sigma_p = \text{diag}(0.03, 0.01, 1.3).$$

For this choice of mean and variance, all quadrature points for a fifth order Gauss-Hermite quadrature approximation of numerical integration were positive. The remaining model parameters are fixed according to Table 1. Next, to fix the likelihood function, the Gaussian noise distribution, i.e., $\varepsilon \sim \mathcal{N}(0, \sigma_z)$, needs to be fixed. To consider reasonable values of σ_z, first the reference peak pyruvate signal is calculated using the low-fidelity model with the default model and data parameters shown in Tables 1 and 2; it is found to be $s_{Pref} = 0.6173$. Then for different signal-to-noise ratios (SNR), the noise (standard deviation) in the individual signals, σ_s, and the standard deviation of the total signal, σ_z, are computed as follows:

$$\sigma_s(SNR) = s_{Pref}/SNR, \qquad \sigma_z(SNR) = \sigma_s\sqrt{2N}, \qquad SNR \in \{2, 5, 10, 15, 20\}, \tag{25}$$

where N is the total number of scans. For each σ_z in the above list, optimal design parameters are obtained by solving the optimization problem (24). For simplicity, let $\mathcal{K}_{OED_{\text{SNR}}}$ denote the optimized design parameter corresponding to $\sigma_z(SNR)$. The rationale behind considering different SNR is that, in reality, data is expected to have varied signal-to-noise ratios and this is shown to impact the choice of optimal design parameters. The initial values of the design parameter $\mathcal{K}$ are listed in Table 2. The number of scans, N, and repetition time, TR_k, are fixed at the initial values. Figures 1 and 2 represent the optimal design parameters, $\mathcal{K}_{OED_{\text{SNR}}}$, for the lower and upper bounds of SNR considered, $SNR = 2$ and $SNR = 20$; respectively. Results show that optimal design parameters vary depending on the SNR values; however, results at $SNR = 2$ and $SNR = 20$ are representative of the range of SNR considered. The optimal values of design parameters are shown in Fig. 1(a), Fig. 1(d), Fig. 2(a) and Fig. 2(d). The time varying optimized design parameters are significantly different from the constant value flip angle scheme. In Fig. 1 and Fig. 2, HP pyruvate and lactate signals, $s_P^k, s_L^k, 1 \le k \le N$, are shown in (b) and (e), respectively. Moreover, in Fig. 1 and Fig. 2, longitudinal magnetizations, $\bar{\phi}_P^k, \bar{\phi}_L^k$, are shown in (c) and (f), respectively.

5.2 Validation of the uncertainty reduction using optimal design parameters

The basic workflow in verification includes generating the samples of noisy data associated with different design parameters using either LF and HF model and then solving the inverse problem for model parameters for each sample of data. From the recovered k_{PL} for different samples of data, the mean and the standard deviation is computed. Specifically, the standard deviation is used as a measure of the uncertainty in the recovered k_{PL}.

Before discussing the results, steps in generating synthetic data are explained. Suppose $\mathcal{K}_{OED_{\text{SNR}}}$ is the optimal design parameter for the noise $\sigma_z(SNR)$ in the total signal, see (25). Using either LF or HF models, "ground truth" (signals at N scans) is generated using $\mathcal{K}_{OED_{\text{SNR}}}$ design parameters (TR_k is fixed following Table 2) and default model parameters listed in Table 1. The data associated to SNR in $\mathcal{K}_{OED_{\text{SNR}}}$ is denoted by $Y_{OED_{SNR}}$ and takes the form:

$$Y_{OED_{SNR}} = \begin{bmatrix} s_P^1 & s_L^1 \\ s_P^2 & s_L^2 \\ . & . \\ . & . \\ s_P^N & s_L^N \end{bmatrix}.$$

In the case in which the LF model is used to generate "ground truth", s_P^i, s_L^i denote the pyruvate and lactate signals at i^{th} scan, see (6). If the data is generated from the HF model, these will be the average pyruvate and lactate signals within a voxel at scan time t_i, see Section 5.2.2 for more details. A total of 25 samples of noisy data for different
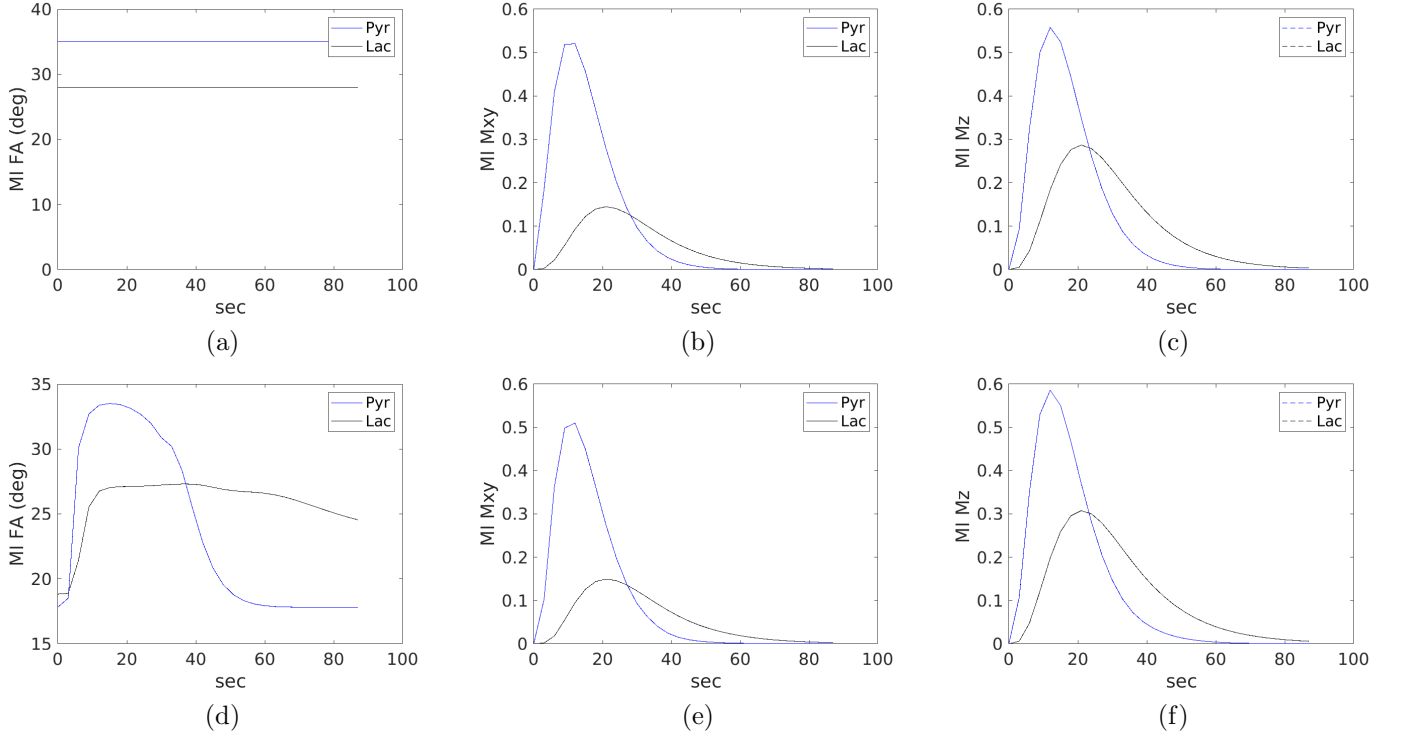
Figure 1: Optimized design parameters along with the solution of the forward (LF) model for noise $\sigma_z(2)$, i.e., $SNR = 2$. The optimized flip angle scheme is shown for (a) constant flip angles throughout the acquisition (optimal angles are $\theta_P^k = 35$ degrees and $\theta_L^k = 28$ degrees, for all $1 \le k \le N$) and (d) allowing the flip angle to vary at each data acquisition. The corresponding signal evolution of the transverse magnetization (6) is shown in (b) for the constant flip angle scheme and (e) for varying flip angles. Similarly, the longitudinal magnetization (1) is shown in (e) for the constant flip angle scheme and (f) for varying flip angles.

values of SNR are considered. Noisy samples are computed as follows:

$$Y_{noisy,OED_{\mathrm{SNR}},SNR_{data}} = f(Y_{OED_{\mathrm{SNR}}}, SNR_{data}) = Y_{OED_{SNR}} + \sigma_s(SNR_{data}) \begin{bmatrix} a_1 & b_1 \\ a_2 & b_2 \\ . & . \\ a_N & b_N \end{bmatrix}, \tag{26}$$

where $\sigma_s(SNR_{data})$, given in (25), is the amount of the noise that depends on the assumed SNR, SNR_{data}, $a_j, b_j \sim \mathcal{N}(0,1)$ for each $j = 1, 2, .., N$. Since the MI optimal solution is seen to vary with respect to SNR defined by the total signal standard deviation, σ_z, and SNR in the data, SNR_{data}, is expected to vary with pixelwise location, a range of added noise values is considered to comprehensively evaluate the accuracy and precision of the k_{PL} parameter recovery. The noise values correspond to the previous SNR range considered: $\sigma_s(SNR_{data}), SNR_{data} \in \{2, 5, 10, 15, 20\}$. Validation results are now presented.

5.2.1 Reduction in uncertainty in k_{PL} for low-fidelity data

The LF model is used to generate data, $Y_{OED_{\mathrm{SNR}}}$ (for SNR = 2, 5, 10, 15, 20), and uncertain parameters $\mathcal{P} = (k_{PL}, k_{ve}, \bar{t}_0)$ in the LF model are recovered from the 25 samples of noisy data. The remaining model parameters are drawn from the Table 1. In Fig. 3, the statistics (mean and standard deviation) corresponding to optimal design parameters shown in Fig. 1 and Fig. 2 is presented. The SNR (SNR to generate noisy data) along the x-axis corresponds to value of $\sigma_s(SNR_{data})$ added to the data. The y-axis represents the mean and standard deviation of the k_{PL} recovered from the inference. The known value of k_{PL} used to generate the noise corrupted data is shown for reference. Figures 3(a) and 3(c) correspond to $\mathcal{K}_{OED_2}$ for a constant and varying flip angle scheme; respectively. Figures 3(b) and 3(d) correspond to $\mathcal{K}_{OED_{20}}$ for a constant and varying flip angle scheme; respectively. Generally, an improvement in the accuracy and precision of the recovered parameter is seen with increasing SNR. The k_{PL} recovered for constant flip angles with $\mathcal{K}_{OED_2}$ shows the best accuracy and precision for the noise corrupted
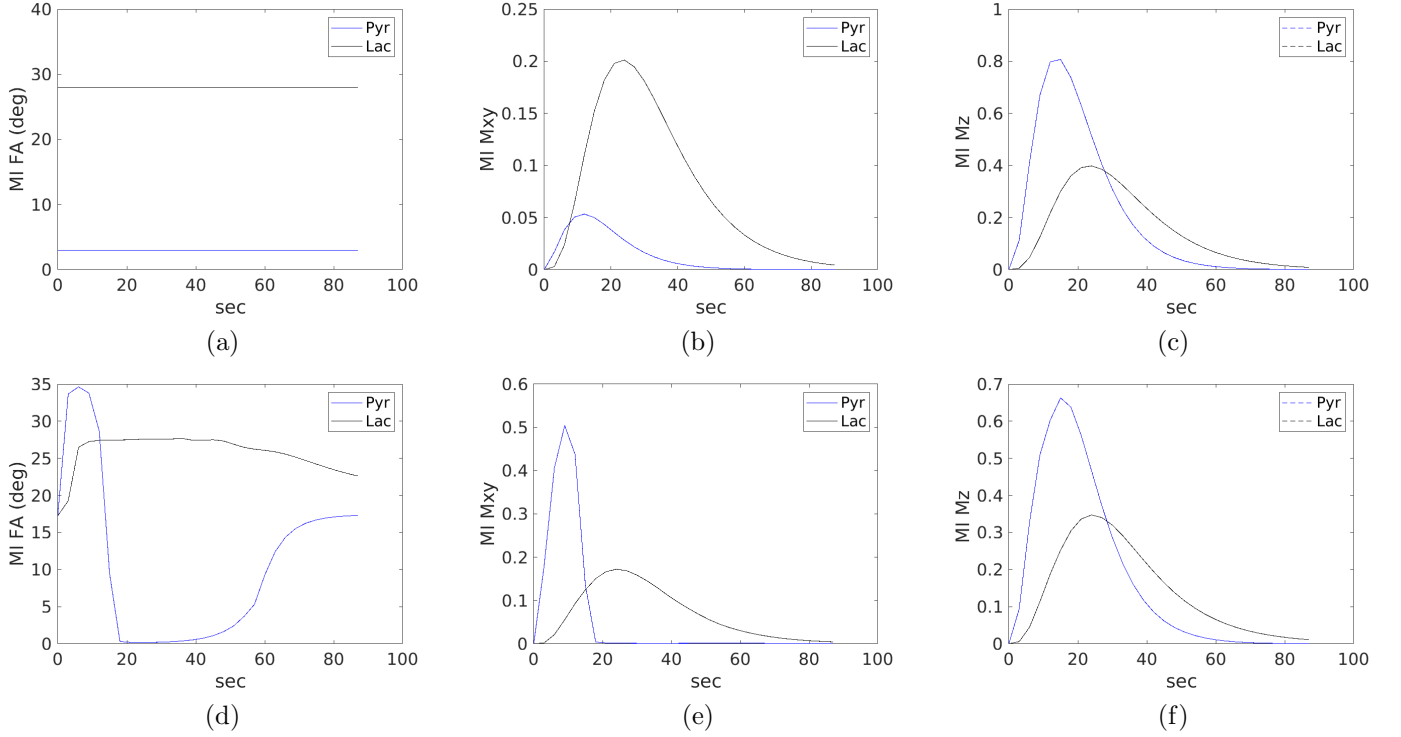
9

Figure 2: Optimized design parameters along with the solution of the forward (LF) model for noise $\sigma_z(20)$, i.e., $SNR = 20$. The optimized flip angle scheme is shown for (a) constant flip angles throughout the acquisition (optimal angles are $\theta_P^k = 3$ degrees and $\theta_L^k = 28$ degrees, for all $1 \le k \le N$) and (d) allowing the flip angle to vary at each data acquisition. The corresponding signal evolution of the transverse magnetization (6) is shown in (b) for the constant flip angle scheme and (e) for varying flip angles. Similarly, the longitudinal magnetization (1) is shown in (e) for the constant flip angle scheme and (f) for varying flip angles.

parameter recovery. Figure 3(e) provides a control for the accuracy and precision obtained for flip angles currently in use in the clinic [44], $\theta_P^k = 20$ and $\theta_L^k = 30$ degrees. Generally, results at $\mathcal{K}_{OED_2}$ are comparable to the current clinical pulse sequence implementation. However, $\mathcal{K}_{OED_2}$ demonstrates improved performance at low $SNR = 2$.

5.2.2 Recovery of rate parameter from the high-fidelity model-based data

A high-fidelity model is used to generate a somewhat more realistic spatially varying data and further verify our results using an independent source of data. In this section, only the k_{PL} parameter is treated as uncertain; all other model parameters were drawn from Table 1.

Consider a cubic domain B containing the brain tissue domain Ω (discretization and simulation using HF model is discussed in Appendix B). Let B_h be a uniform discretization of B with total 16^3 cells. First, the HF model is simulated using the constant design parameter $\mathcal{K}_{OED_{SNR}}$ for $SNR = 2$, i.e., $\theta_P^k = 35$ degrees and $\theta_L^k = 28$ degrees, for all $1 \le k \le N$, while all other parameters are fixed from Table 1 and Table 2. For the high-fidelity calculations, only constant $\mathcal{K}_{OED_2}$ design parameter set was employed for the reasons that $\mathcal{K}_{OED_2}$ is found to be more robust for large ranges of noises and the values in $\mathcal{K}_{OED_2}$ are closer to what is currently being considered in clinical testing; see previous subsection. Next, the total pyruvate and lactate signals, $s_P^k, s_L^k, 1 \le k \le N$, are computed over each cell of B_h, i.e., Y_{OED_2} at different cells of B_h is obtained. Suppose $Y_{OED_{SNR}}^I$, $1 \le I \le 16^3$, is the data for I^{th} cell in grid B_h. Then, given the $SNR_{data} \in [2, 5, 10, 15, 20]$, the noisy data from $Y_{OED_2}^I$ for the Ith cell is computed using

$$Y_{noisy,OED_{\text{SNR}},SNR_{data}}^I = Y_{OED_{SNR}}^I + \sigma_s^I(SNR_{data}) \begin{bmatrix} a_1 & b_1 \\ a_2 & b_2 \\ . & . \\ a_N & b_N \end{bmatrix}, \tag{27}$$

where $\sigma_s^I(SNR_{data}) = \frac{s_{P_{ref}}^I}{SNR_{data}}$, $s_{P_{ref}}^I$ is the maximum pyruvate signal (maximum value in the first column of
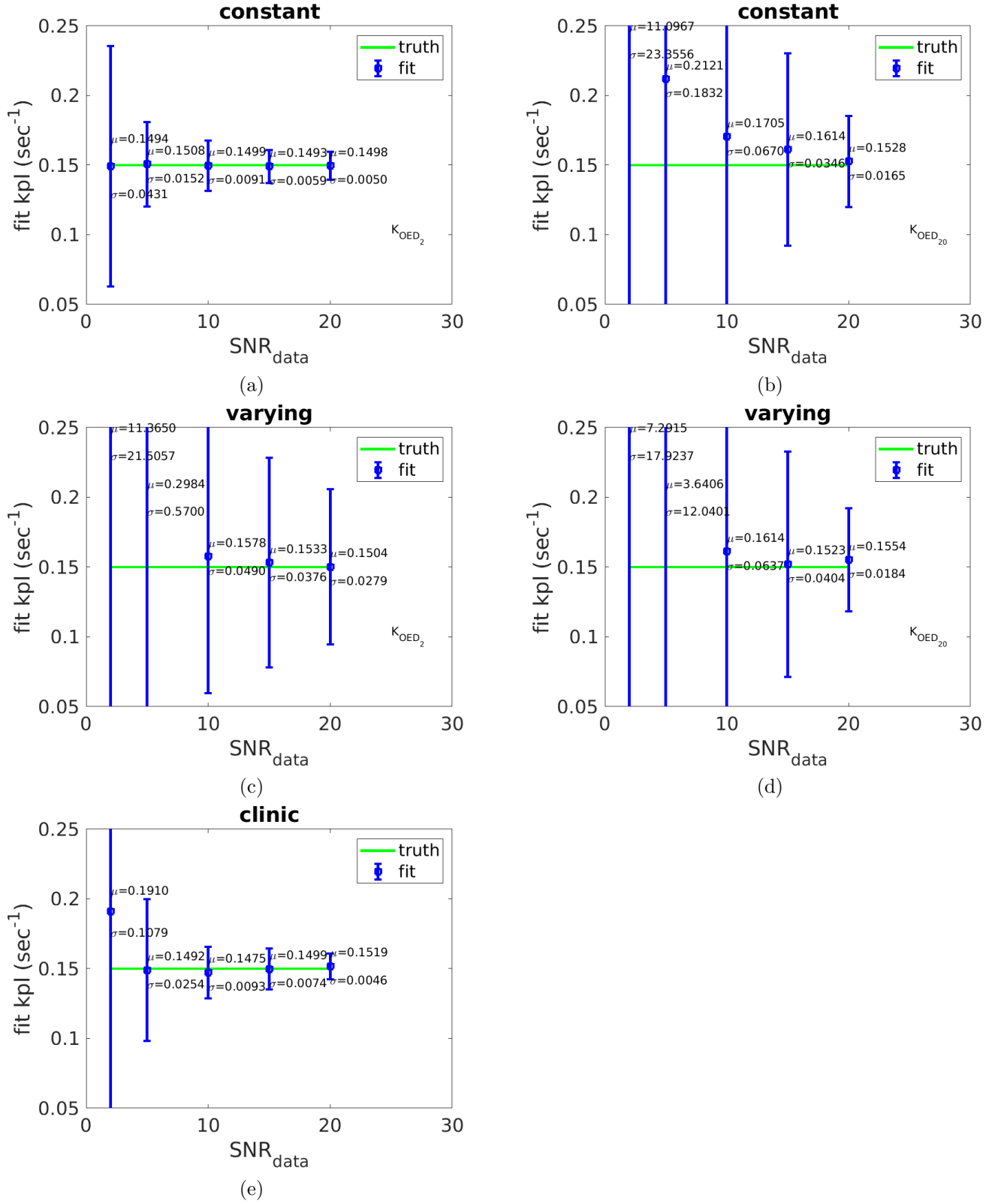
Figure 3: Plot of inferred k_{PL} from 25 samples of noisy data obtained from LF model data. The x-axis is the value of SNR_{data} corresponding to value of noise, $\sigma_s(SNR_{data})$, added to the synthetic data for inference. (a) and (c) correspond to $\mathcal{K}_{OED_2}$ for a constant and varying flip angle scheme; respectively. (b) and (d) correspond to $\mathcal{K}_{OED_{20}}$ for a constant and varying flip angle scheme; respectively. (e) provides a control for the accuracy and precision obtained for flip angles currently used in human studies. Flip angles currently in use in the clinic are $\theta_P^k = 20$ and $\theta_L^k = 30$.

11

$Y^I_{OED_{SNR}}$) for the Ith cell, and a_i, b_i, c_i, d_i are defined similar to (26). Essentially, the noise model in this case varies from cell to cell and is scaled appropriately depending on the peak pyruvate signal for a given cell. The HP signals can be very small in many cells; peak signal in cells can be as small as 0.01 based on simulation results. Therefore, adding noise $\sigma_s(SNR_{data}) = s_{Pref}/SNR_{data}$ based on one fixed reference signal $s_{Pref} = 0.6173$, see (25), to data corresponding to cells with small peak pyruvate signal will produce meaningless results.

Range	Number of cells	Range	Number of cells
[1., 0.1)	7	[0.1, 0.01)	12
[0.01, 0.001)	4	[0.001, 0)	2

Table 3: Four ranges of peak vascular pyruvate is considered to capture the variation in the uncertainty of parameters as cells move further from the vascular sources.

Since it is expensive to solve an inverse problem on each cell in B_h for all ranges of SNR_{data}, 25 cells in B_h are selected based on the peak value of HP pyruvate in the vascular compartment to solve an inverse problem. A total of four ranges of peak vascular pyruvate are considered and cells such that peak vascular pyruvate of the cell, $\max_k \bar{\phi}_{PV}(t_k)$, is in the range is selected. The range and number of selected cells are provided in Table 3. Here, $\bar{\phi}_{PV}$ is the average of vascular pyruvate over a given cell. Vascular pyruvate is nonzero only on $x \in \Omega_V$, where Ω_V is the vascular domain segmented from the MRI data, see (13). Thus the average vascular pyruvate will vary from cell to cell depending on the magnitude of the the intersection between Ω_V and the cell. The composition of cells based on the strength of vascular pyruvate agent is essential to capture the variations in the uncertainty of recovered parameters both near and far from the vascular sources.

In Fig. 4, the mean and standard deviation of inferred k_{PL} for different cells and different SNR_{data} values are shown. Here, only one design parameter set, $\mathcal{K}_{OED_2}$, is considered. The X-axis in Fig. 4 identifies the cell number (total 25 cells are considered) while in the Y-axis the mean (on top plot) and standard deviation (on bottom plot) of recovered k_{PL} are displayed. Different colors signify different values of SNR_{data}. 'Noiseless k_{PL}' is the one that is obtained by solving an inverse problem on data from specific cells without adding noise.

From Fig. 4, the following key observations can be made:

- **Decrease in the uncertainty with decreasing noise in the data**: The smaller $\sigma_s(SNR_{data})$ results in smaller overall uncertainty in the recovered k_{PL}. Further, the recovered k_{PL} from noisy data are seen to converge to the noiseless k_{PL} obtained without the addition of any noise.

- **Uncertainty is stronger for cells with high peak vascular pyruvate**: In cells with stronger vascular pyruvate, the uncertainty in recovered k_{PL} is higher. In fact as the peak vascular pyruvate in cells decrease (cell number low to high), the recovered k_{PL}, e.g., mean k_{PL} in the Fig. 4, gets closer to the $k_{PL} = 0.15$ employed in the high-fidelity simulation. Therefore, the results suggest that in the cells with high impact from a vascular source, the inconsistency between the high-fidelity model and low-fidelity is higher. Since in a real HP-MRI measurement, any given cell may include the convection and diffusion effects, and therefore the fitting of data using the ODE-based pharmacokinetic models which ignore these effects will likely lead to less accurate results.

6 Discussion

Within the mutual information based optimal experimental design formulation, a time varying flip angle scheme is seen to provide significant differences in the flip angles as compared to the case when excitation angles are fixed to a constant value. Indeed, the varying flip angle scheme leads to a higher parameter optimization that is able to further improve the quantitative value of mutual information over the constant flip angle scheme. However, as seen in Fig. 3, the constant flip angle scheme leads to the best accuracy and precision when considering the inference from noise-corrupted data. The time varying flip angle scheme is seen to be most sensitive to noise corruption of the expected signal and is generally seen to have the highest variance and bias in the parameter recovery.

The reduction in the recovered variance is seen to be correlated with the assumed noise value added to the data. Intuitively, less noise resulted in less variance in the parameter recovery. Less intuitively, the optimal MI solutions for flip angles are seen to vary with the noise value of the signal conditional probability model. The greatest reduction in measurement uncertainty is seen for the MI optimal solution corresponding to low SNR. The excitation angles optimized for the higher SNR condition drop the pyruvate excitation angle to zero after 20 seconds while simultaneously increasing the lactate flip angle. This is in contrast to the low SNR case where both pyruvate
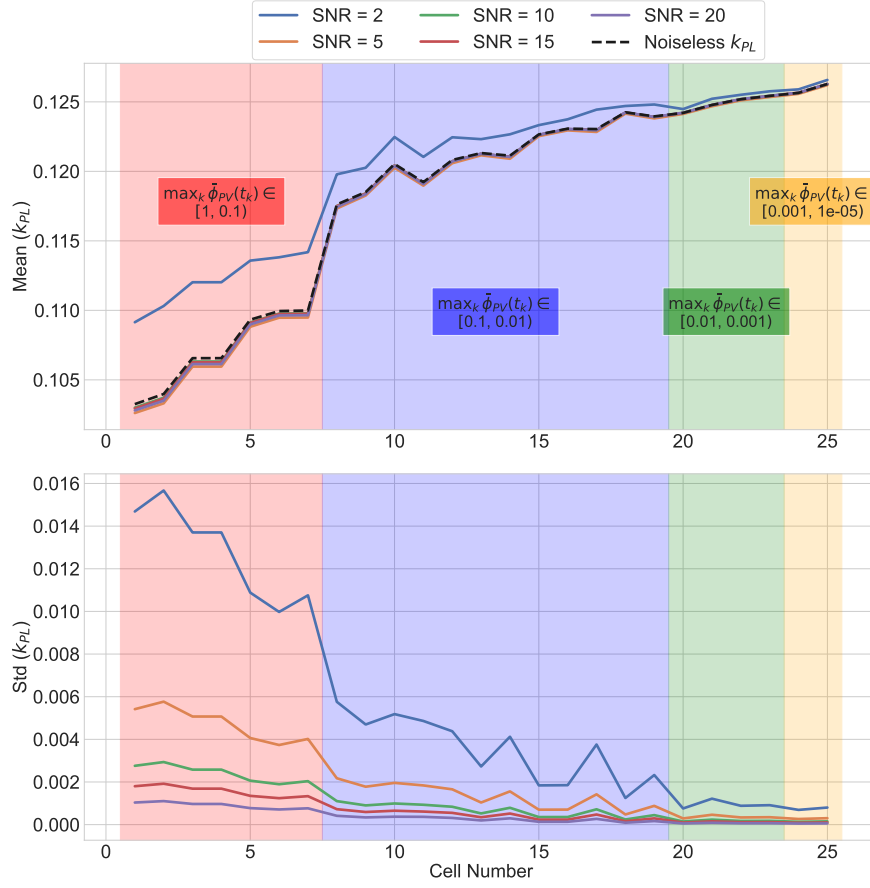
Figure 4: Plot of the mean and standard deviation of inferred k_{PL} for 25 selected cells in 16^3 grid. On x-axis, the cells are numbered and on y-axis the value of the mean and standard deviation for specific cells are plotted. Cells were selected based on the peak vascular pyruvate, $\max_k \bar{\phi}_{PV}(t_k)$, where $\bar{\phi}_{PV}$ is the average of vascular pyruvate over a given cell, belonging to four range of values as shown in the plot. Color of each curve is related to the SNR_{data} used in computing noisy data.

and lactate flip angles maintain an continual signal. This could be due to the system being so signal limited for the low SNR case that it is forced to leverage the pyruvate signal to extract any additional information about the metabolic exchange rate. As opposed to the high SNR case where the abundant lactate signal is sufficient to accurately determine the metabolic exchange rate and measuring pyruvate signal after the initial bolus is therefore unnecessarily.

This work also highlights some issues observed when using the high-fidelity spatially varying model generated "ground truth" in recovering the model parameters in the low-fidelity spatially invariant model. The recovered parameters of the low-fidelity model are not same as the values considered in generating "ground truth"; further this difference is higher at locations with stronger vascular pyruvate source. Thus, this work shows that it is possible that the difference between k_{PL} in real tissue and the k_{PL} values recovered using the low-fidelity model could be large.

This work considers uncertainty in the vascular-tissue exchange parameter, bolus arrival time, and rate constants. However, a more comprehensive evaluation of additional uncertain parameters would be to additionally consider the stability of our results. The numerical computation in this work is also limited by the quadrature scheme for numerical integration of the mutual information integrals. Adding additional sources of uncertainty suffers from the well-known curse of dimensionality [45] and alternative integration schemes such as Markov chain Monte Carlo may be more effective.

Further, the current approach assumes a SNR such that Gaussian statistics is an appropriate noise model for the the signal acquisition. Rician statistics [46] is known to be more appropriate as the noise model for low SNR and will be considered in future efforts to optimize acquisition parameters at low SNR. The low SNR range is expected to be more important toward the end of the HP data acquisition as the signal decays.

Alternative high-fidelity models may also be considered to determine optimal design parameters and to recover model parameters from the data. However, for such an approach to work, a realistic high-fidelity model is needed

13

keeping in mind the major factors in HP-MRI physics. This work presents a high-fidelity model based on various simplifying assumptions as a first step. Moreover, the model in this work was limited to just two constituents. Additional model fidelity may include permutations of lactate and pyruvate that are endogenous as well as hyperpolarized. Intravascular, extracellular, and intracellular species may also be considered. Additional formulations may also consider the impact of blood flow in the simulations directly though Dirichlet boundary conditions, as convective transport through porous media [47], or as a sophisticated 3D-1D coupling with vasculature treated as 1D curvilinear segments [48, 49].

In summary, our results suggest that the constant flip angle scheme corresponding to $\mathcal{K}_{OED_2}$ is the best choice in terms of accuracy and precision of the parameter recovery. Results at $\mathcal{K}_{OED_2}$, $\theta_P^k = 35$ and $\theta_L^k = 28$, are comparable to the current clinical pulse sequence implementations, $\theta_P^k = 20$ and $\theta_L^k = 30$, and demonstrate an improved performance at low $SNR_{data} = 2$. Further, the constant flip angle scheme may represent a practical choice for implementation on the pulse sequence hardware.

Acknowledgments

References

[1] Sarah J Nelson, John Kurhanewicz, Daniel B Vigneron, Peder EZ Larson, Andrea L Harzstark, Marcus Ferrone, Mark Van Criekinge, Jose W Chang, Robert Bok, Ilwoo Park, et al. Metabolic imaging of patients with prostate cancer using hyperpolarized [1-13c] pyruvate. *Science translational medicine*, 5(198):198ra108–198ra108, 2013.

[2] J.A. Bankson, C.M. Walker, M.S. Ramirez, W. Stefan, D. Fuentes, M.E. Merritt, J. Lee, V.C. Sandulache, Y. Chen, L. Phan, P.-C. Chou, A. Rao, S.-C.J. Yeung, M.-H. Lee, D. Schellingerhout, C.A. Conrad, C. Malloy, A.D. Sherry, S.Y. Lai, and J.D. Hazle. Kinetic modeling and constrained reconstruction of hyperpolarized [1-13C]-pyruvate offers improved metabolic imaging of tumors. *Cancer Research*, 75(22), 2015.

[3] John Kurhanewicz, Daniel B Vigneron, Jan Henrik Ardenkjaer-Larsen, James A Bankson, Kevin Brindle, Charles H Cunningham, Ferdia A Gallagher, Kayvan R Keshari, Andreas Kjaer, Christoffer Laustsen, et al. Hyperpolarized 13c mri: path to clinical translation in oncology. *Neoplasia*, 21(1):1–16, 2019.

[4] Kristin L Granlund, Sui-Seng Tee, Hebert A Vargas, Serge K Lyashchenko, Ed Reznik, Samson Fine, Vincent Laudone, James A Eastham, Karim A Touijer, Victor E Reuter, et al. Hyperpolarized mri of human prostate cancer reveals increased lactate with tumor grade driven by monocarboxylate transporter 1. *Cell metabolism*, 31(1):105–114, 2020.

[5] Vesselin Z Miloushev, Kayvan R Keshari, and Andrei I Holodny. Hyperpolarization mri: preclinical models and potential applications in neuroradiology. *Topics in magnetic resonance imaging: TMRI*, 25(1):31, 2016.

[6] Vesselin Z Miloushev, Kristin L Granlund, Rostislav Boltyanskiy, Serge K Lyashchenko, Lisa M DeAngelis, Ingo K Mellinghoff, Cameron W Brennan, Vivian Tabar, T Jonathan Yang, Andrei I Holodny, et al. Metabolic imaging of the human brain with hyperpolarized 13c pyruvate demonstrates 13c lactate production in brain tumor patients. *Cancer research*, 78(14):3755–3760, 2018.

[7] Rahul Aggarwal, Daniel B Vigneron, and John Kurhanewicz. Hyperpolarized 1-[13c]-pyruvate magnetic resonance imaging detects an early metabolic response to androgen ablation therapy in prostate cancer. *European urology*, 72(6):1028, 2017.

[8] Ferdia A Gallagher, Ramona Woitek, Mary A McLean, Andrew B Gill, Raquel Manzano Garcia, Elena Provenzano, Frank Riemer, Joshua Kaggie, Anita Chhabra, Stephan Ursprung, et al. Imaging breast cancer using hyperpolarized carbon-13 mri. *Proceedings of the National Academy of Sciences*, 117(4):2092–2098, 2020.

[9] Ramona Woitek, Mary A McLean, Andrew B Gill, James T Grist, Elena Provenzano, Andrew J Patterson, Stephan Ursprung, Turid Torheim, Fulvio Zaccagna, Matthew Locke, et al. Hyperpolarized 13c mri of tumor metabolism demonstrates early metabolic response to neoadjuvant chemotherapy in breast cancer. *Radiology: Imaging Cancer*, 2(4):e200017, 2020.

[10] Otto Warburg. On the origin of cancer cells. *Science*, 123(3191):309–314, 1956.

[11] Matthew G Vander Heiden, Lewis C Cantley, and Craig B Thompson. Understanding the warburg effect: the metabolic requirements of cell proliferation. *science*, 324(5930):1029–1033, 2009.

[12] James T Grist, Mary A McLean, Frank Riemer, Rolf F Schulte, Surrin S Deen, Fulvio Zaccagna, Ramona Woitek, Charlie J Daniels, Joshua D Kaggie, Tomasz Matys, et al. Quantifying normal human brain metabolism using hyperpolarized [1–13c] pyruvate and magnetic resonance imaging. *NeuroImage*, 189:171–179, 2019.

[13] Casey Y Lee, Hany Soliman, Benjamin J Geraghty, Albert P Chen, Kim A Connelly, Ruby Endre, William J Perks, Chris Heyn, Sandra E Black, and Charles H Cunningham. Lactate topography of the human brain using hyperpolarized 13c-mri. *NeuroImage*, 204:116202, 2020.

[14] Adam W Autry, Jeremy W Gordon, Lucas Carvajal, Azma Mareyam, Hsin-Yu Chen, Ilwoo Park, Daniele Mammoli, Maryam Vareth, Susan M Chang, Lawrence L Wald, et al. Comparison between 8-and 32-channel phased-array receive coils for in vivo hyperpolarized 13c imaging of the human brain. *Magnetic resonance in medicine*, 82(2):833–841, 2019.

[15] Christopher M Walker, David Fuentes, Peder EZ Larson, Vikas Kundra, Daniel B Vigneron, and James A Bankson. Effects of excitation angle strategy on quantitative analysis of hyperpolarized pyruvate. *Magnetic resonance in medicine*, 81(6):3754–3762, 2019.

[16] John Maidens, Peder EZ Larson, and Murat Arcak. Optimal experiment design for physiological parameter estimation using hyperpolarized carbon-13 magnetic resonance imaging. In *2015 American Control Conference (ACC)*, pages 5770–5775. IEEE, 2015.

[17] John Maidens, Jeremy W Gordon, Murat Arcak, and Peder EZ Larson. Optimizing flip angles for metabolic rate estimation in hyperpolarized carbon-13 mri. *IEEE transactions on medical imaging*, 35(11):2403–2412, 2016.

[18] GJ Marseille, R De Beer, M Fuderer, AF Mehlkopf, and D van Ormondt. Bayesian estimation of mr images from incomplete raw data. In *Maximum Entropy and Bayesian Methods*, pages 13–22. Springer, 1996.

[19] Oscar Brihuega-Moreno, Frank P Heese, and Laurance D Hall. Optimization of diffusion measurements using cramer-rao lower bound theory and its application to articular cartilage. *Magnetic resonance in medicine*, 50(5):1069–1076, 2003.

[20] Dirk HJ Poot, Arnold J den Dekker, Eric Achten, Marleen Verhoye, and Jan Sijbers. Optimal experimental design for diffusion kurtosis imaging. *Medical Imaging, IEEE Transactions on*, 29(3):819–829, 2010.

[21] Mara Cercignani and Daniel C Alexander. Optimal acquisition schemes for in vivo quantitative magnetization transfer mri. *Magnetic resonance in medicine*, 56(4):803–810, 2006.

[22] Stanley J Reeves and Zhao Zhe. Sequential algorithms for observation selection. *Signal Processing, IEEE Transactions on*, 47(1):123–132, 1999.

[23] Shihao Ji, Ya Xue, and Lawrence Carin. Bayesian compressive sensing. *Signal Processing, IEEE Transactions on*, 56(6):2346–2356, 2008.

[24] Matthias Seeger, Hannes Nickisch, Rolf Pohmann, and Bernhard Schölkopf. Optimization of k-space trajectories for compressed sensing by bayesian experimental design. *Magnetic resonance in medicine*, 63(1):116–126, 2010.

[25] Thomas M Cover and Joy A Thomas. *Elements of information theory*. John Wiley & Sons, 2012.

[26] J Tinsley Oden, Andrea Hawkins, and Serge Prudhomme. General diffuse-interface theories and an approach to predictive tumor growth modeling. *Mathematical Models and Methods in Applied Sciences*, 20(03):477–517, 2010.

[27] Beatrice Riviere. *Discontinuous Galerkin methods for solving elliptic and parabolic equations: theory and implementation*. SIAM, 2008.

[28] Donald W Peaceman. *Fundamentals of numerical reservoir simulation*. Elsevier, 1977.

[29] Charles R Faust and James W Mercer. Geothermal reservoir simulation: 1. mathematical models for liquid-and vapor-dominated hydrothermal systems. *Water resources research*, 15(1):23–30, 1979.

[30] Thomas Gerstner and Michael Griebel. Numerical integration using sparse grids. *Numerical Algorithms*, 18:209–232, 1998.

[31] H. Niederreiter. *Random Number Generation and Monte Carlo Methods*. 1992.

[32] Christian Robert and George Casella. *Monte Carlo statistical methods*. Springer Science & Business Media, 2013.

[33] Sanford Gordon and Bonnie J McBride. *Computer program for calculation of complex chemical equilibrium compositions and applications*. Citeseer, 1996.

[34] I H Sloan, S Joe, and S.L.M.S. Joe. *Lattice Methods for Multiple Integration*. Oxford science publications. Clarendon Press, 1994.

[35] Alan Genz. *A Package for Testing Multiple Integration Subroutines*, pages 337–340. Springer Netherlands, Dordrecht, 1987.

[36] Paul van Dooren and Luc de Ridder. An adaptive algorithm for numerical integration over an n-dimensional cube. *Journal of Computational and Applied Mathematics*, 2(3):207–217, 1976.

[37] Andrew R. Barron. Approximation and Estimation Bounds for Artificial Neural Networks. *Machine Learning*, 14(1):115–133, 1994.

[38] DR Daniel R Cavagnaro, JI Jay I Myung, Mark a Pitt, and Janne V JV Kujala. Adaptive design optimization: A mutual information-based approach to model discrimination in cognitive science. *Neural computation*, 22(1956):1–15, 2010.

[39] Christopher C. Drovandi, James M. McGree, and Anthony N. Pettitt. A sequential Monte Carlo algorithm to incorporate model uncertainty in Bayesian sequential design. *Journal of Computational and Graphical Statistics*, 23(1):3–24, 2014.

[40] Elizabeth G. Ryan, Christopher C. Drovandi, M. Helen Thompson, and Anthony N. Pettitt. Towards Bayesian experimental design for nonlinear models that require a large number of sampling times. *Computational Statistics and Data Analysis*, 70:45–60, 2014.

[41] Kenneth J Ryan. Estimating Expected Information Gains for Experimental Designs With Application to the Random Fatigue-Limit Model. *Journal of Computational and Graphical Statistics*, 12(3):585–603, 2003.

[42] Elizabeth G. Ryan, Christopher C. Drovandi, James M. Mcgree, and Anthony N. Pettitt. A Review of Modern Computational Algorithms for Bayesian Optimal Design. *International Statistical Review*, 84(1):128–154, 2016.

[43] Drew P Mitchell, Ken-Pin Hwang, James A Bankson, R Jason Stafford, Suchandrima Banerjee, Naoyuki Takei, and David Fuentes. An information theory model for optimizing quantitative magnetic resonance imaging acquisitions. *Physics in Medicine & Biology*, 65(22):225008, 2020.

[44] Shuyu Tang, Maxwell V Meng, James B Slater, Jeremy W Gordon, Daniel B Vigneron, Bradley A Stohr, Peder EZ Larson, and Zhen Jane Wang. Metabolic imaging with hyperpolarized 13c pyruvate magnetic resonance imaging in patients with renal tumorsinitial experience. *Cancer*, 127(15):2693–2704, 2021.

[45] Stefan Berchtold, Christian Böhm, and Hans-Peter Kriegal. The pyramid-technique: Towards breaking the curse of dimensionality. In *Proceedings of the 1998 ACM SIGMOD international conference on Management of data*, pages 142–153, 1998.

[46] Hákon Gudbjartsson and Samuel Patz. The rician distribution of noisy mri data. *Magnetic resonance in medicine*, 34(6):910–914, 1995.

[47] D Fuentes, E Thompson, M Jacobsen, A Colleen Crouch, RR Layman, B Riviere, and E Cressman. Imaging-based characterization of convective tissue properties. *International Journal of Hyperthermia*, 37(3):155–163, 2020.

[48] Marvin Fritz, Prashant K. Jha, Tobias Köppl, J. Tinsley Oden, and Barbara Wohlmuth. Analysis of a new multispecies tumor growth model coupling 3d phase-fields with a 1d vascular network. *Nonlinear Analysis: Real World Applications*, 61:103331, 2021.

[49] Marvin Fritz, Prashant K Jha, Tobias Köppl, J Tinsley Oden, Andreas Wagner, and Barbara Wohlmuth. Modeling and simulation of vascular tumors embedded in evolving capillary networks. *Computer Methods in Applied Mechanics and Engineering*, 384:113975, 2021.

[50] Bjoern H Menze, Andras Jakab, Stefan Bauer, Jayashree Kalpathy-Cramer, Keyvan Farahani, Justin Kirby, Yuliya Burren, Nicole Porz, Johannes Slotboom, Roland Wiest, et al. The multimodal brain tumor image segmentation benchmark (brats). *IEEE transactions on medical imaging*, 34(10):1993–2024, 2014.

[51] Brian B Avants, Nicholas J Tustison, Jue Wu, Philip A Cook, and James C Gee. An open source multivariate framework for n-tissue segmentation with evaluation on public data. *Neuroinformatics*, 9(4):381–400, 2011.

[52] Alejandro F Frangi, Wiro J Niessen, Koen L Vincken, and Max A Viergever. Multiscale vessel enhancement filtering. In *International conference on medical image computing and computer-assisted intervention*, pages 130–137. Springer, 1998.

[53] Nobuyuki Otsu. A threshold selection method from gray-level histograms. *IEEE transactions on systems, man, and cybernetics*, 9(1):62–66, 1979.

[54] Martin S. Alnæs, Jan Blechta, Johan Hake, August Johansson, Benjamin Kehlet, Anders Logg, Chris Richardson, Johannes Ring, Marie E. Rognes, and Garth N. Wells. The fenics project version 1.5. *Archive of Numerical Software*, 3(100), 2015.

[55] Anders Logg, Kent-Andre Mardal, Garth N. Wells, et al. *Automated Solution of Differential Equations by the Finite Element Method*. Springer, 2012.

A   Development of a high-fidelity model for HP-MRI

Let $\Omega \subset \mathbb{R}^3$ represent a three-dimensional tissue domain and let $\Omega_V \subset \Omega$ is the part of the tissue occupied by the vascular structure. Consider an RVE (Representative Volume Element) of sub-tissue length scale (≈ 1 mm) at some point $\boldsymbol{x} \in \Omega$. A simple depiction of RVE is shown in Fig. 5 which highlights three key compartments, namely, interstitial, vascular, and cellular. Suppose V is the total volume of RVE, and V_i, V_v, and V_c are the volumes of interstitial, vascular, and cellular compartments, respectively, such that $V = V_i + V_v + V_c$. Further, let $\sigma_a = V_a/V$, $a \in \{i, v, c\}$, give the volume fractions of compartments.

While each compartment may consist of variety of constituents, HP pyruvate and lactate in the interstitial and vascular compartments are of particular interest. Let $\phi_P = V_P/V$ and $\phi_L = V_L/V$ denote the volume fraction of HP pyruvate and lactate in interstitium (V_P, V_L are the volumes of HP agents in the interstitial compartment of an RVE) while $\phi_{\sim PL}$ giving the volume fraction of all other constituents in the interstitial compartment. Volume fractions in vascular compartment, $\phi_{PV}, \phi_{LV}, \phi_{\sim PLV}$, and in cellular compartment, $\phi_{PC}, \phi_{LC}, \phi_{\sim PLC}$, are defined in a similar fashion. For a generic RVE, following saturation condition must hold, i.e.,

$$\phi_P + \phi_L + \phi_{\sim PL} = \sigma_i = \frac{V_i}{V}.$$

Similarly, constituents in vascular and cellular compartments must satisfy

$$\phi_{PV} + \phi_{LV} + \phi_{\sim PLV} = \sigma_v = \frac{V_v}{V}, \qquad \phi_{PC} + \phi_{LC} + \phi_{\sim PLC} = \sigma_c = \frac{V_c}{V}.$$

Constituent volume fractions defined above present a difficulty in the sense that, for example, ϕ_P, at a point $\boldsymbol{x} \in \Omega$ depend on σ_i due to saturation condition, and therefore spatial variation of σ_i (and similarly σ_v, σ_c) is needed. To avoid this difficulty, $\sigma_i, \sigma_v, \sigma_c$ are assumed to be constant (spatially and temporally), and ϕ_A for constituent A in interstitial compartment is defined as $\phi_A = V_A/V_i$ for $A \in \{P, L, \sim PL\}$. Constituents in other two compartments are defined similarly. With this, saturation conditions become

$$\sum_{A \in \{P,L,\sim PL\}} \phi_A = 1, \qquad \sum_{A \in \{PV,LV,\sim PLV\}} \phi_A = 1, \qquad \sum_{A \in \{PC,LC,\sim PLC\}} \phi_A = 1.$$
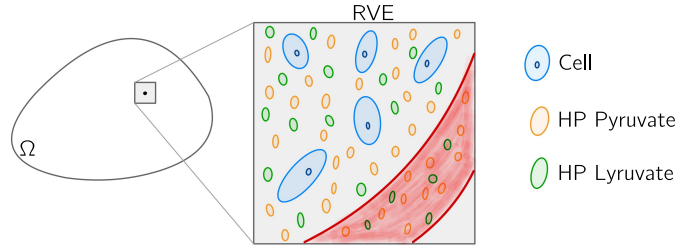
Figure 5: Schematics of an RVE at sub-tissue scale with basic constituents and compartments.

Key assumptions To derive PDE-based model of HP agents, some simplifying assumptions will be made. The key assumptions are:

(A1) Cellular compartment and constituents within it are ignored; however, the extension to include this compartment is straight-forward;

(A2) Tissue domain is treated as homogeneous media and properties such as diffusivities are assumed to be uniform;

(A3) HP agents in vascular compartment are fixed and given. HP pyruvate in vascular compartment, ϕ_{PV}, is spatially uniform and varies in time following the gamma probability density function on Ω_V subdomain of Ω. HP lactate in vascular compartment, ϕ_{LV}, is fixed to zero;

(A4) Perfusion of HP agents is simulated using volume source terms in the balance of mass of HP agents in interstitium. Perfusion is restricted to subdomain Ω_V. Further, exchange of mass is considered one-way, i.e., HP agents perfuse from vascular to interstitial compartment and not in the other direction;

(A5) The mechanical and thermal effects are ignored. This is a realistic assumption as typically HP-MRI measurements take place over a short time interval (≈ 100 seconds) and mechanical effects over this short interval can be safely ignored;

(A6) In the balance of mass of constituents in interstitium, besides the reaction between HP agents and natural loss of signal, agents are assumed to diffuse. Convection effects are ignored. This may not be a realistic assumption as the time scale of measurements suggest that perfusion from capillaries and convection are dominant mechanism for mobility of agents as compared to the diffusion. Future work may address this limitation in the model; and

(A7) The signal loss due to excitation is assumed to be instantaneous (reasonable assumption considering the time interval of one scan and overall time interval of simulation).

B   Numerical methods for forward simulation and MI optimization

In this section, the numerical discretization of the HP-MRI model (mainly HF model) and numerical implementation of the optimization problem to determine optimal design parameters are discussed. To solve the LF model presented in Section 3.1, a MATLAB function `ode45` is employed. Numerical discretization of the HF model is discussed next.

B.1   Discretization of the HF model

The HF model is applied to real brain tissue; the sample data is taken from the publicly available BRATS brain MRI datasets [50]. The vascular domain Ω_V was extracted from the MRI data in several steps: First, a four component Gaussian mixture model [51] was applied to the subtraction image of the difference between the pre- and post-contrast T1-weighted imaging. Hessian-based [52] filters were applied to the posterior image class with the brighted intensity. Otsu thresholding [53] is applied to extract the foreground vessel mask. Finally, a 4×4 axial plane dilation is applied as a post processing step to oversegment the vessels and ensure smaller vessels were simply connected. In Fig. 6, the vascular segmentation (a) and the finite element mesh of the brain tissue (b) are shown.

The coupled PDEs in (8) are discretized using finite element method and a implicit first order time discretization. Let $V_h \subset H^1(\Omega)$ denote the finite element space spanned by a second order shape functions over conforming tetrahedral triangulation of Ω. Let $\phi_{Pn}^k, \phi_{Ln}^k, \phi_{PVn}^k, \phi_{LVn}^k \in V_h$ denote the finite element solution at the nth time step at time $\tau_n = t_k + n\Delta t_k$, where Δt_k is a time step size in interval $[t_k, t_{k+1})$ (Δt_k can vary with k). Suppose
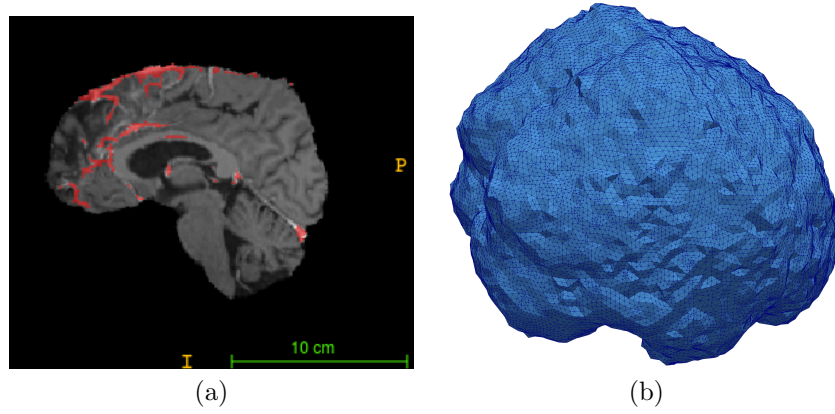
Figure 6: (a) Brain T1 contrast enhanced MRI with segmented vascular (red regions). The vascular regions represent Ω_V. The MRI data consists of 240×240×155 voxels. In (b), a finite element mesh of the tissue is depicted.

$\phi_P^{k-1}(t_{k-1}), \phi_L^{k-1}(t_{k-1}) \in V_h$ are already computed and known. Then the initial condition ϕ_{P0}^k, ϕ_{L0}^k are applied using (9):

$$\left(\phi_{P0}^k, \tilde{\phi}\right) = \left(\cos(\theta_P^{k-1})\phi_P^{k-1}(t_{k-1}), \tilde{\phi}\right), \qquad \left(\phi_{L0}^k, \tilde{\phi}\right) = \left(\cos(\theta_L^{k-1})\phi_L^{k-1}(t_{k-1}), \tilde{\phi}\right), \qquad \forall \tilde{\phi} \in V_h. \qquad (28)$$

As discussed in Section 3.2, HP agents in the vascular domain, $\phi_{PVn}^k, \phi_{LVn}^k$, for all $n = 0, 1, .., N_k$, are fixed and given via relation (13). Suppose solution $\phi_{Pn-1}^k, \phi_{Ln-1}^k$ at the $(n-1)^{\text{th}}$ step are known. To determine ϕ_{Pn}^k, ϕ_{Ln}^k, we consider a implicit discretization as follows (noting that $k_{LP} = 0$ and $\phi_{LVn}^k = 0$ for all k and n), for all $\tilde{\phi} \in V_h$,

$$\left(\frac{\phi_{Pn}^k - \phi_{Pn-1}^k}{\Delta t_k}, \tilde{\phi}\right) + \left(D_P \nabla \phi_{Pn}^k, \nabla \tilde{\phi}\right) - \left(\left[-\frac{1}{T_{1,P}} - k_{PL}\right]\phi_{Pn}^k, \phi_P^k\right) = \left(L_P \phi_{PVn}^k \chi_{\Omega_V}, \tilde{\phi}\right) \qquad (29)$$

and

$$\left(\frac{\phi_{Ln}^k - \phi_{Ln-1}^k}{\Delta t_k}, \tilde{\phi}\right) + \left(D_L \nabla \phi_{Ln}^k, \nabla \tilde{\phi}\right) - \left(-\frac{1}{T_{1,L}}\phi_{Ln}^k - k_{PL}\phi_{Pn}^k, \tilde{\phi}\right) = 0. \qquad (30)$$

Observe that the above two equations can be decoupled by solving (29) first and then solving (30).

Next, the convergence of numerical discretization is established.

B.1.1 Time and mesh convergence study

To compare the solution from different mesh and time steps, finite element solutions of problem over a brain tissue is projected onto a uniform mesh with $N_h = 16^3$ cubic elements, denoted by B_h, of cubic domain B, where B is the smallest cube containing Ω. Next, at any simulation time t, for each cell K_i in B_h, the total volume of HP agents are computed; suppose $Q_P^i(t), Q_L^i(t)$ denotes the total volume of pyruvate and lactate at time t for the i cell in B_h. Suppose $Q_{P,1}^i, Q_{P,2}^i$ and $Q_{L,1}^i, Q_{L,2}^i$, for all i, are results from two simulations, then, the total error in HP pyruvate and lactate at time t is defined as

$$e_P^{1,2}(t) = \frac{1}{\sqrt{|K|}}\sqrt{\sum_{1 \leq i \leq N_h} |Q_{P,1}^i(t) - Q_{P,2}^i(t)|^2}, \qquad e_L^{1,2}(t) = \frac{1}{\sqrt{|K|}}\sqrt{\sum_{1 \leq i \leq N_h} |Q_{L,1}^i(t) - Q_{L,2}^i(t)|^2}, \qquad (31)$$

where $|K| = 1042.672$ is the volume of one element in B_h.

The high-fidelity model was solved approximately using FEniCS library [54, 55]. In the convergence results presented below, model parameters are taken from Table 1 while the design parameters are taken as, for $1 \leq k \leq N = 30$, $\theta_P^k = 35$ and $\theta_L^k = 28$ degrees, respectively (these parameters are the OED parameters for SNR $= 2$, see Fig. 1). Repetition times are $TR_k = 3$ seconds, for $2 \leq k \leq N$.

To verify the convergence of solver with decreasing time-step sizes, model was solved with a fixed mesh consisting of 333049 elements and 68991 vertices and different time steps Δt_k. Time steps employed in this study are $\Delta t_k = \{0.6, 0.3, 0.15, 0.075\}$ seconds for all k. Simulation with largest $\Delta t_k = 0.4$ is labeled as 1 and the one with smallest $\Delta t_k = 0.05$ is labeled 4. The errors as defined in (31) for pair of simulations are shown in Fig. 7. The error is seen to decrease consistently with the decreasing time step.

To ascertain mesh convergence, model was solved with a fixed time step $\Delta t_k = 0.075$ seconds and four difference meshes. The number of tetrahedral elements and vertices in four meshes employed in this study are: $(239697, 48695)$, $(333049, 68991)$, $(404492, 84991)$, $(523746, 108276)$. Results with coarsest mesh (smaller number of elements) is labeled as 1 while the one with finest mesh is labeled as 4. The errors for different pair of simulations are shown in Fig. 8. The error is seen to decrease as the mesh is refined.

Based on the time and mesh convergence results, to compute "ground truth", the mesh with 239697 elements and 48695 vertices is employed and the time step is fixed to $\Delta t_k = 0.15$ seconds.
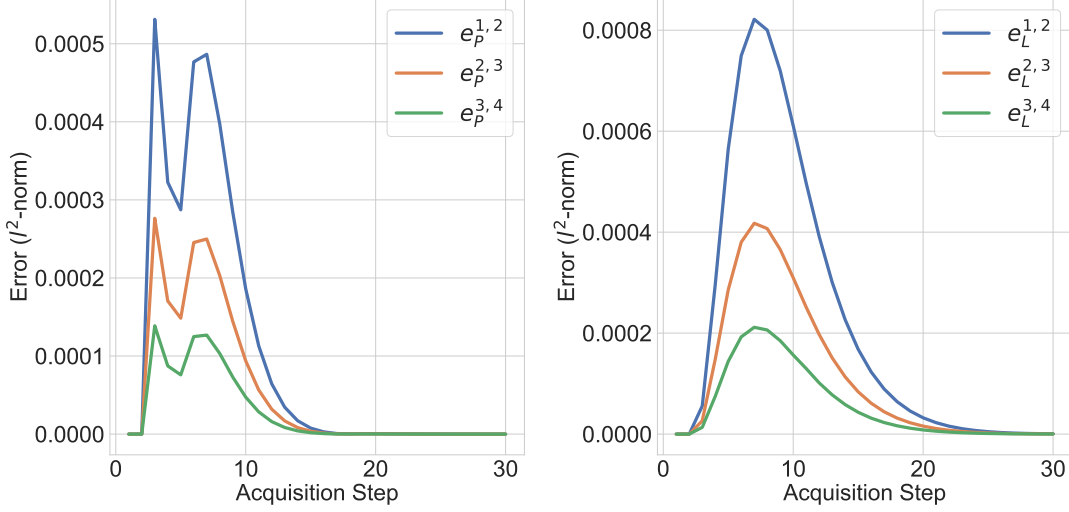

Figure 7: Plot of errors for pair of simulations at scan times $t_k = (k-1) * 3$ seconds, $1 \le k \le 30$. Simulation with $\Delta t_k = 0.6$ seconds is labeled as 1 and the one with $\Delta t_k = 0.075$ seconds as 4, and the errors for pair of simulations are computed using (31). The relative error is seen to decrease as time step is decreased.
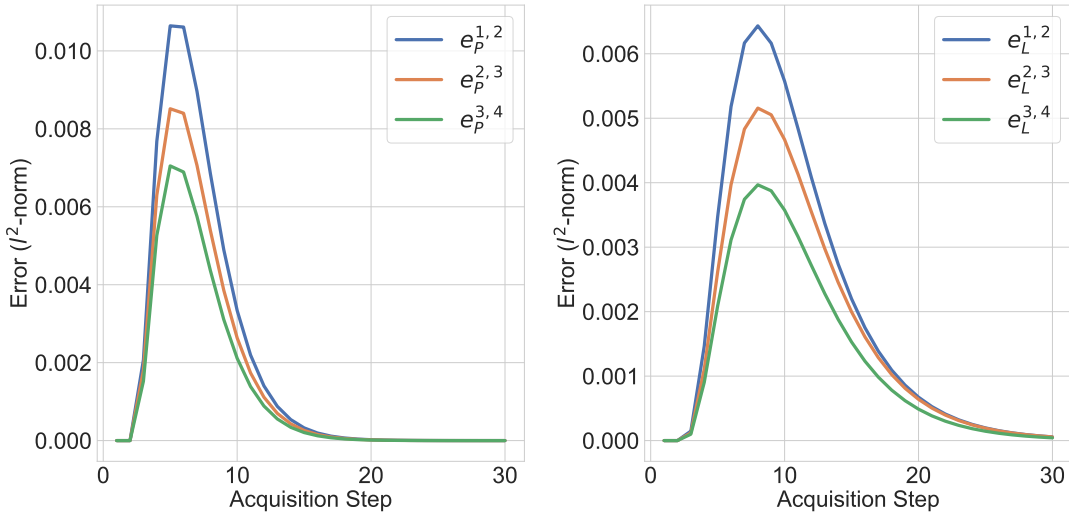

Figure 8: Plot of errors for pair of simulations at scan times $t_k = (k-1) * 3$ seconds, $1 \le k \le 30$. Four simulations are carried out each with different mesh keeping the time step fixed to $\Delta t_k = 0.075$ seconds; simulation 1 corresponds to the coarsest mesh and simulation 4 corresponds to the finest mesh. The relative errors are seen to decrease as the mesh is refined.

B.2 Automatic differentiation accelerated optimization for OED calculations

The auto-differentiation functions of MATLAB were used to calculate gradients of (21). In particular, design parameters $\mathcal{K}$ and state variables $\bar{\phi}$ were considered as optimization variables to minimize the objective function (21)

with respect to the model constraints (1). Auto-differentiation provides the derivatives of the objective function and constraints with respect to this full space formulation. Given the derivatives in the full space formulation, the reduced space gradient of the objective function (21) with respect to the design parameters $\mathcal{K}$ may be calculated using an adjoint solve.

B.3 Inverse problem to recover rate parameter

A MATLAB routine `fmincon` is used to solve the inverse problem of recovering model parameters $\mathcal{P}$ in the LF model (1) from the data. Signals of pyruvate and lactate at different scans is taken as data. As an objective function for the inverse problem, square of the difference between data and model prediction of signals is used. Similarly, derivatives from the automatic differentiation feature in the MATLAB are utilized for numerical optimization.